Electronic Supplementary Material (ESI) for Nanoscale.

Supplementary Information for:

Reconfigured far-field coherent thermal emission using mid-infrared bilayer metasurfaces.

Sichao Li [a], Robert E Simpson [b], Sunmi Shin * [a]

[a.] Department of Mechanical Engineering, Collage of Design and Engineering, National University of Singapore, 9 Engineering Drive 1, 117575, Singapore.

E-mail: mpeshin@nus.edu.sg

[b.] School of Engineering, University of Birmingham, Edgbaston, B15 2TT, UK

Supplementary Note 1: *Detailed Information on Fabrication Process*

The detailed fabrication process can be obtained with following schematic. We want to highlight that during all the fabrication steps the temperature was strictly controlled under the phase change temperature (around 420 K) including PR baking, DRIE etching and metal deposition. Also, as the crystallinity will increase the electrical conduction for the GST layer, which may cause the leakage with our metal beams, we added pre-etching for the GST around the Pt electrodes pattering areas to make sure the disconnection of the Pt to GST.

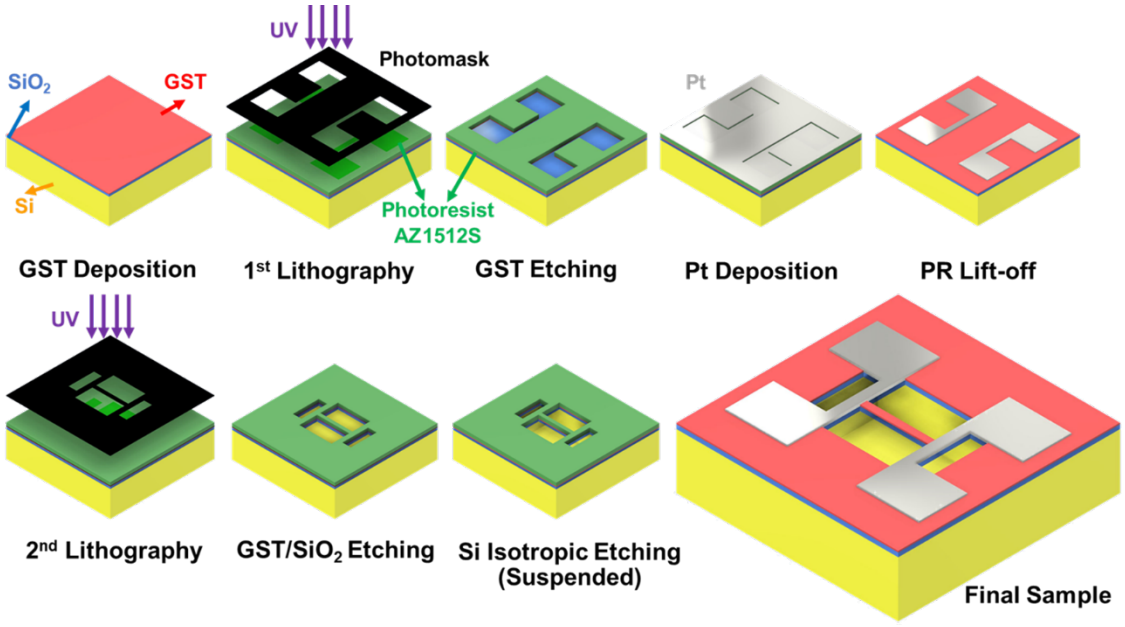

Figure S1. Schematics of sample fabrication process. To highlight, before we deposit Pt to fabricate the electrodes, we did pre-etching for the GST beneath the Pt to make sure the Pt electrodes are discontinuous from the GST layer. It can avoid the direct electrical leakage from Pt to GST.

Supplementary Note 2: *Temperature Distribution and Frequency Controlled L_P along the sample.*

The temperature profile along the sample length in our measurement is only affected by the thermal conduction and radiation as convection is negligible in our ultra-high vacuum chamber (< 10^{-6} Torr). In between, the weight of thermal radiation is corelated to the emission

area, which is determined by the length of sample (considering same width and thickness). Therefore, temperature profile for short sample with minor emission area will be overlapped with the blue line with only consideration on conduction, while longer sample with high weight of radiation due to the large emission area can follow the red line with lower temperature increase at sensing side. In this case, with multiple samples at different lengths, we can summarize the thermal emissivity value. However, it method with multiple measurement and fabrication can be much time and money consuming. Therefore, L_P control with frequency change can be more efficient. With low frequency applied on one long sample, $L_P >> L$ which makes the heat fully penetrated along the entire sample length to simultaneously have the effective emission area to be the entire surface area. By increase the heating frequency, L_P is reduced which decreases the effective area contributing to thermal emission. This frequency controlled modulation gives an alternative way to effectively change the relative contribution from conduction and radiation – which can be the same as length dependent study with multiple sample lengths.

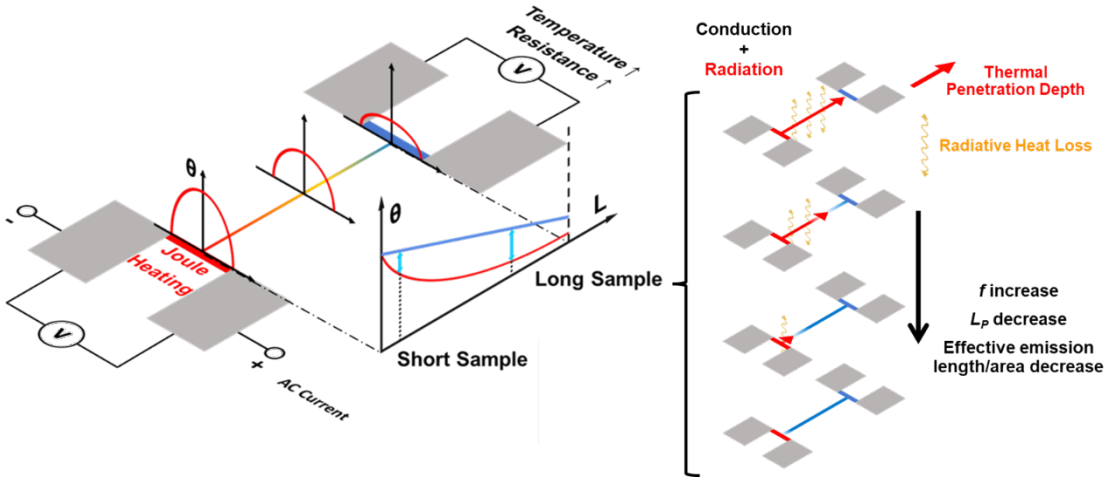

Figure S2. Ideal temperature distribution for samples in ultra-high vacuum (negligible convection). For short sample with smaller effective emission area, pure conduction would be dominant (blue line); while for longer sample with larger emission area and more radiative heat loss, temperature distribution would be dominant by both conduction and radiation (red line). In our experiment, we control the L_P by control the heating frequency. For our long NR sample, by increasing the frequency from low to high, L_P decreases from fully penetrate to partially penetrate and finally no penetration.

During this process, the effective emission length/area are dynamically controlled, which in other word, realizes the effective length dependent study.

Supplementary Note 3: *Modelling Results with c-GST layer.*

Similar with the a-GST/SiO_2 cases we mentioned in main manuscript, modelling results on c-GST/SiO_2 structure are also plotted for comparison. Less energy confinement and larger red shift are obtained by additional c-GST thin layer due to the high contrast of dielectric constant between the a- and c-GST.

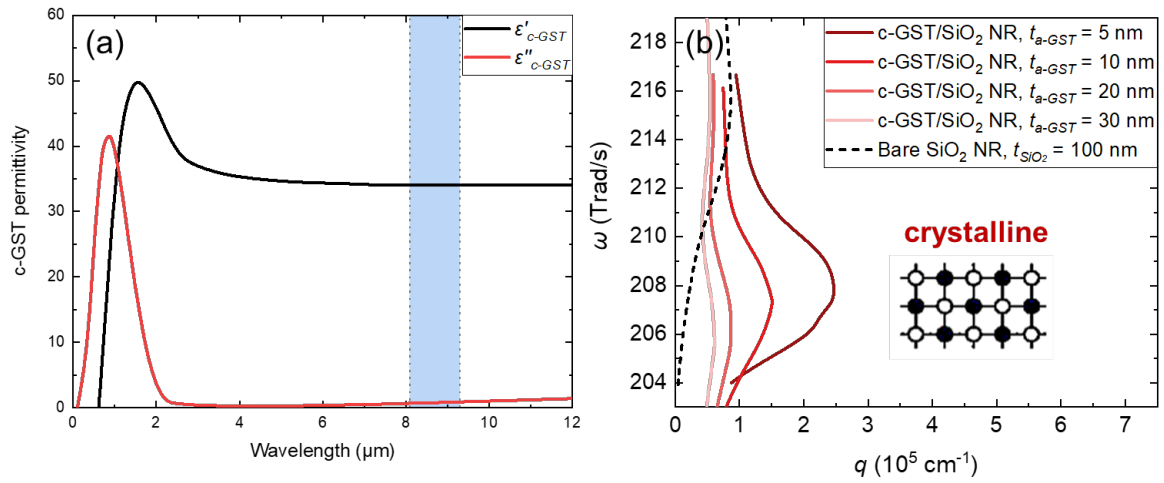

Figure S3. (a) Wavelength dependent dielectric constant of c- GST we used for our calculations[1]. (b) Dispersions of various thickness (5 to 30 nm) of c-GST covered nanoribbon calculated by our numerical modelling.

Supplementary Note 4: *Fitted Parameters in Calculation of Dielectric Constant of GST Material.*

Table S1. Fitting parameters for the Drude modified Tauc–Lorentz dispersion model[2].

Fitting Parameters		
Parameters	**Amorphous**	**Crystalline**
$\boldsymbol{\Gamma}$	1.00 x 10^{15}	3.84 x 10^{15}
$\boldsymbol{\omega_p}$	9.31 x 10^{4}	1.15 x 10^{15}
$\boldsymbol{A_{TL}}$	2.48	1.45
$\boldsymbol{E_0}$	142.30	242.18
$\boldsymbol{C}$	4.14	2.48
$\boldsymbol{E_g}$	0.71	0.50

Supplementary Note 5: *Uncertainty Analysis of Thermal Conductivity Measurement.*

The apparent thermal conductivity is calculated by the sample conductance and geometric parameter given by $\kappa = \frac{GL}{A}$, where A is the cross-sectional area determined by width (W) and thickness (t). Using the uncertainty propagation rule, the error of can be expressed as

$$\left(\frac{\delta\kappa}{\kappa}\right)^2 = \left(\frac{\delta G}{G}\right)^2 + \left(\frac{\delta L}{L}\right)^2 + \left(\frac{\delta W}{W}\right)^2 + \left(\frac{\delta t}{t}\right)^2$$

where δ is the uncertainty, $\left(\frac{\delta t}{t}\right)$ is less than 2% from the commercial thermal oxide wafer, $\left(\frac{\delta L}{L}\right)$ and $\left(\frac{\delta W}{W}\right)$ are determined by the alignment of photolithograph and measured by SEM, which has been confirmed to be less than 4% and 3%, respectively. Since the sample conductance is calculated by $G = \frac{Q\theta_s}{\theta_h(\theta_h - \theta_s)}$, where Q is the heat applied on the heating beam $(= I_{AC}^2 R_h)$. The error in G can be expressed as

$$\left(\frac{\delta G}{G}\right)^2 = \left(\frac{\delta Q}{Q}\right)^2 + \left(\frac{\delta \theta_h}{\theta_h}\right)^2 + \left(\frac{\delta \theta_s}{\theta_s}\right)^2 + \left(\frac{\delta(\theta_h - \theta_s)}{(\theta_h - \theta_s)}\right)^2$$

$$\left(\frac{\delta Q}{Q}\right)^2 = \left(2\frac{\delta I_{AC}}{I_{AC}}\right)^2 + \left(\frac{\delta R_h}{R_h}\right)^2$$

where both $\left(\frac{\delta I}{I}\right)$ and $\left(\frac{\delta R_h}{R_h}\right)$ are less than 1% and 2% by our measurement setup, respectively. The major uncertainty is from the θ_s calculated by the electrical signal, which can be expressed by

$$\left(\frac{\delta \theta_s}{\theta_s}\right)^2 = \left(\frac{\delta V_s}{V_s}\right)^2 + \left(\frac{\delta R_s}{R_s}\right)^2 + \left(\frac{\delta \alpha_s}{\alpha_s}\right)^2$$

The $\left(\frac{\delta \alpha_s}{\alpha_s}\right)$ is mainly determined by the $\left(\frac{\delta R_s}{R_s}\right)$ and cryostat temperature fluctuation (~50 mK)[3, 4], which can result in less than 5% error range of $\left(\frac{\delta \alpha_s}{\alpha_s}\right)$. Large noise level of $\left(\frac{\delta V_s}{V_s}\right)$ can be observed for long sample measurement with low frequency used (e.g., ~ 10 nV low frequency noise for the 800 μm $Ge_2Sb_2Te_5/SiO_2$ NR, resulting in ~25% of $\frac{\delta \theta_s}{\theta_s}$). Therefore, the additional error range of the thermal conductivity for 800 μm $Ge_2Sb_2Te_5/SiO_2$ NR at high temperatures can be up to 38% - which has been shown in Fig. 3(c).

Supplementary Note 6: *Stefan-Boltzmann Distribution at Different Temperatures.*

SPhPs are still active to enhance the emissivity, but the thermal emitting power would reduce as the intensity is proportional to ~T^3 at low temperatures. The broadband nature of thermal energy at finite temperatures follows the Stefan-Boltzmann distribution with the dominant thermal energy peaks at 9.7 μm and 14.2 μm at 300 K and 200 K, respectively. As shown in Fig. S5, the Reststrahlen band is effectively located within the thermal spectrum corresponding to 300 K and 200 K. Furthermore, we observed further enhanced emissivity at lower temperatures down to 100 K, which confirms the stronger resonant effect with the suppression of phonon broadening and increased phonon lifetime at low temperatures. The observation is consistent to the enhanced far-field radiation study by Thompson et al[5] where the enhanced ratio to the blackbody limit increases at lower temperatures down to 100 K.

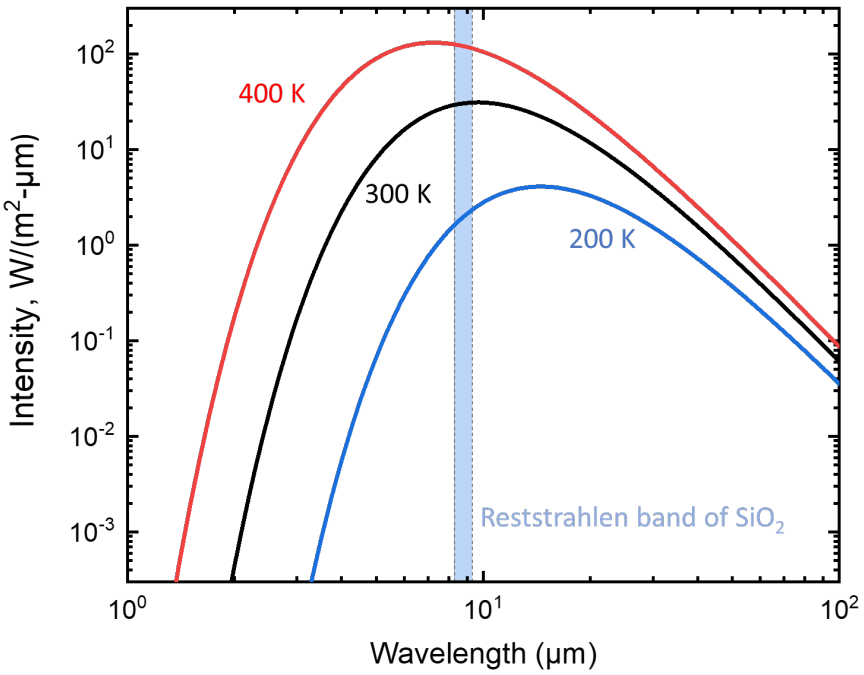

Figure S4. Blackbody spectrum determined by the Stefan-Boltzmann distribution at 200, 300 and 400 K, which both overlapped with the Reststrahlen band of SiO_2 near to the peak intensity.

Supplementary Note 7: *Normalized Spectral Absorption Cross-sectional Area of 5 μm Wide $Ge_2Sb_2Te_5/SiO_2$ Nanoribbon.*

We conducted 2D numerical modelling[6] to calculate the normalized spectral absorption cross-sectional area of 5 μm wide $Ge_2Sb_2Te_5/SiO_2$ nanoribbon $\left(\sigma_{abs}/\sigma_{geom}\right)$ as shown in Fig. S5, which can be used to understand the spectral distribution of the coherent emission. One can clearly see that strong enhancement at the resonant frequencies (ω_{LO} and ω_{TO}) The results indicate that other dispersive modes outside the Reststrahlen band (e.g., bulk phonon polaritons with dispersion close to light-line) make insignificant contributions on the thermal emission enhancement.

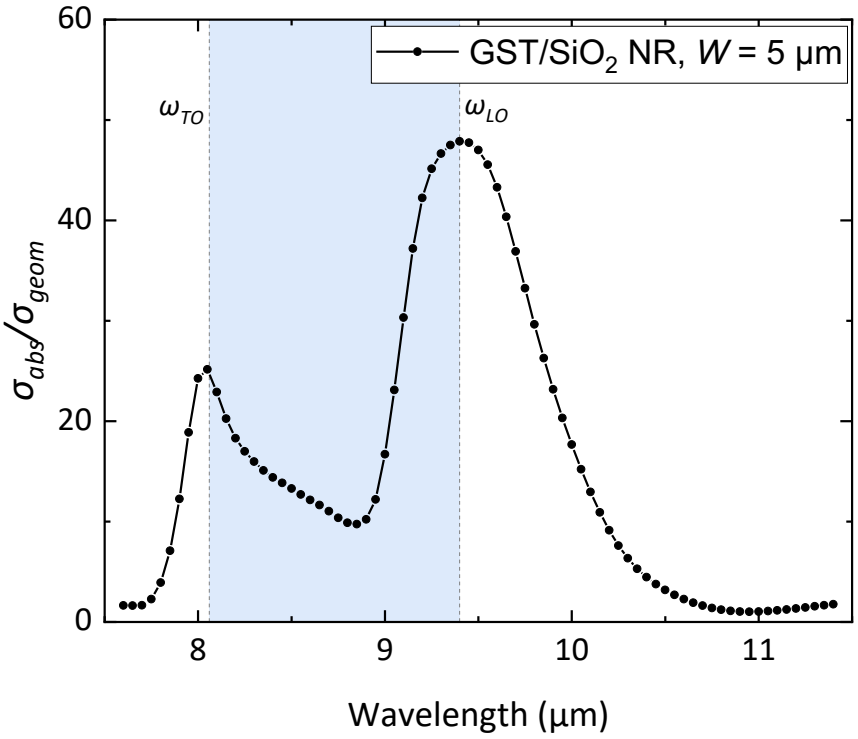

Figure S5. Enhanced absorption cross-sectional area of 5 μm wide $Ge_2Sb_2Te_5/SiO_2$ nanoribbon as a function of wavelength, where the absorption cross-sectional area (σ_{abs}) is normalized by the geometrical cross-section (σ_{geom}).

References:

1. L. T. Chew, W. Dong, L. Liu, X. Zhou, J. Behera, H. Liu, K. V. Sreekanth, L. Mao, T. Cao and J. Yang, 2017.
2. B.-S. Lee, J. R. Abelson, S. G. Bishop, D.-H. Kang, B.-k. Cheong and K.-B. Kim, *Journal of Applied Physics*, 2005, **97**, 093509.
3. R. Shrestha, P. Li, B. Chatterjee, T. Zheng, X. Wu, Z. Liu, T. Luo, S. Choi, K. Hippalgaonkar and M. P. De Boer, *Nature communications*, 2018, **9**, 1664.
4. J. Zhu, K. Hippalgaonkar, S. Shen, K. Wang, Y. Abate, S. Lee, J. Wu, X. Yin, A. Majumdar and X. Zhang, *Nano letters*, 2014, **14**, 4867-4872.
5. D. Thompson, L. Zhu, R. Mittapally, S. Sadat, Z. Xing, P. McArdle, M. M. Qazilbash, P. Reddy and E. Meyhofer, *Nature*, 2018, **561**, 216-221.
6. S. Shin, M. Elzouka, R. Prasher and R. Chen, *Nat Commun*, 2019, **10**, 1377.